

ROSAT PSPC X-ray observations of the nearby spiral galaxy M83

M. Ehle^{1,2,3}, W. Pietsch¹, R. Beck², U. Klein⁴

¹ Max-Planck-Institut für Extraterrestrische Physik, Giessenbachstraße, 85740 Garching, Germany

² Max-Planck-Institut für Radioastronomie, Auf dem Hügel 69, 53121 Bonn, Germany

³ Australia Telescope National Facility, P.O. Box 76, Epping N.S.W. 2121, Australia

⁴ Radioastronomisches Institut der Universität Bonn, Auf dem Hügel 71, 53121 Bonn, Germany

Received 23 October 1995/ Accepted 9 June 1997

Abstract. The nearly face-on SBc galaxy M83 (NGC 5236) was observed for 25 ksec with the *ROSAT* PSPC. We detected 13 point-like sources in this galaxy, 10 of which were previously unknown, down to a limiting luminosity of $\sim 0.8 \cdot 10^{38}$ erg s⁻¹ (for D=8.9 Mpc). Eight of these sources are positionally associated with H II regions and/or H I voids, suggesting an association with the younger stellar population, variable X-ray binaries or with hot expanding gaseous bubbles.

We measured extended X-ray radiation from almost the whole optically visible galaxy with a luminosity of $L_x \sim 3.6 \cdot 10^{40}$ erg s⁻¹ in the energy range 0.1-2.4 keV. Approximately 20% of this emission can be explained by undetected point-like sources. We detected diffuse soft (0.1-0.4 keV) X-ray emission due to hot gas with a luminosity of $L_x(\text{soft}) \sim 1.4 \cdot 10^{40}$ erg s⁻¹. Comparing the diffuse soft and hard X-ray emission components, we observed a different asymmetric distribution and a slower radial decrease of the intensity profile of the soft X-ray emission. Both these results support the existence of a huge spherical gas halo of $\sim 10 - 15$ kpc radius. On the other hand, the radial scale lengths of the hard X-ray radiation, that of the thermal radio emission and the profile of the optical surface brightness are similar, favouring the idea that all these emission processes are connected to star formation in the galaxy's disk.

M83 is the first face-on galaxy where the diffuse X-ray emission spectrum can be characterized by a two-temperature thermal plasma: a soft X-ray emitting warm 'halo component' of plasma temperature $2.1 \cdot 10^6$ K and an internally absorbed hot 'disk component' at $5.7 \cdot 10^6$ K which is dominating the emission in the hard (0.5-2.0 keV) *ROSAT* energy range. The (distance-independent) mean surface brightness of the soft diffuse emission of M83 is about twice that of NGC 253.

The electron densities in the galactic halo of M83 ($\sim 1.2 \cdot 10^{-3} / \sqrt{\eta}$ cm⁻³, with a volume filling factor η) are in general too low to explain the observed depolarization of the radio emission. This indicates that the ionization equilibrium might be violated, leading to higher electron densities. The combination of X-ray and radio polarization observations allows an estimate of the plasma parameter $\beta = U_{\text{therm}}/U_{\text{magn}}$ which is found to be 0.2 ± 0.1 . This result supports the hypothesis that magnetic fields play an important role for the evolution and structure of galactic gas haloes. The high energy input rate in the active star-forming disk of M83 seems to be responsible for the outflow of hot gas and the halo formation.

Key words: Galaxies: individual: M83, haloes, ISM – ISM: general, magnetic fields – X-rays: galaxies

1. Introduction

The nearby spiral galaxy M83 (NGC 5236) is a classical grand-design spiral located at a distance of 8.9 Mpc¹. It has been the target of numerous astrophysical investigations in various spectral regimes because of its proximity. Table 1 lists some general parameters of M83.

M83 was first observed in X-rays with the *Einstein* observatory Imaging Proportional Counter (IPC) as part of a sample of nearby spiral galaxies to study their integrated properties (Fabbiano et al. 1984). Trinchieri et al. (1985) obtained high-resolution X-ray observations with the *Einstein* HRI and detected three unresolved sources and a nuclear component.

¹ Distance determinations of M83 have come up with rather different values; here we adopt that of Sandage & Tammann (1975) and scale all luminosities to that value

Table 1. Parameters for M83 (NGC 5236)

Parameter	Value	Reference and Comments
Type	SBc(s)II	Sandage & Tammann (1987; RSA)
R.A. (J2000)	13 ^h 37 ^m 0 ^s .25	Condon et al. (1982), central radio source
Decl. (J2000)	−29°51′51″.3	Condon et al. (1982), central radio source
Position angle of major axis	45°	Talbot et al. (1979)
Inclination	24°	Talbot et al. (1979)
Distance	8.9 Mpc	Sandage and Tammann (1975)
		10'' $\hat{=}$ 0.43 kpc
Size (D_{25})	29 kpc	de Vaucouleurs et al. (1976)
Total mass	$1 - 5 \cdot 10^{11} M_{\odot}$	Huchtmeier & Bohnenstengel (1981), derived from rotation curve
H I mass	$2.4 \cdot 10^{10} M_{\odot}$	Huchtmeier & Bohnenstengel (1981), integrated over the extent of the H I distribution (76' \times 94'6)
Abs. blue magnitude	−21.7 $\hat{=}$ $2.8 \cdot 10^{44}$ erg/s	RSA Catalog of Bright Galaxies
X-ray luminosity	$3.2 \cdot 10^{40}$ erg/s	<i>Einstein</i> IPC (0.5-3.0) keV, Trinchieri et al. (1985)
	$4.2 \cdot 10^{40}$ erg/s	<i>Einstein</i> HRI (0.5-3.0) keV, Trinchieri et al. (1985)
	$4.5 \cdot 10^{40}$ erg/s	<i>Ginga</i> (2-10) keV, Ohashi et al. (1990)
	$5.7 \cdot 10^{40}$ erg/s	<i>ROSAT</i> PSPC (0.1-2.4) keV, this work

The starburst nucleus of M83 is a strong X-ray source that was detected in the *Einstein* observations with a luminosity of $L_x \sim 1 \cdot 10^{40}$ erg s^{−1}. Trinchieri et al. (1985) suggested that the X-ray emission from the nucleus is not dominated by a contribution of massive binary star systems, but is due to a less evolved X-ray emitting population. They also discussed the possibility that a large fraction of the X-ray emission from the nucleus of M83 could be produced by thermal emission from hot shock-heated gas ejected from the nucleus, as is detected in NGC 1068 (Wilson et al. 1992), M82 (Watson et al. 1984) and NGC 253 (Fabbiano & Trinchieri 1984, Fabbiano 1988, Pietsch 1993). A further peculiarity of the nuclear region of M83 is the existence of a polar, circum-nucleus dust lane probably in a plane tilted from the galactic plane by about 70° (Sofue & Wakamatsu 1994). Reducing the accretion to the nucleus, this ring structure might affect the nuclear star-forming activity.

The *Einstein* IPC observations indicated an X-ray extent comparable in size and shape to that seen in blue light. This emission component was discussed as probably due to faint individual sources (evolved stellar population, LMXBs), distributed uniformly across the disk of the galaxy (Trinchieri et al. 1985).

Ohashi et al. (1990) observed M83 in the harder X-ray energy band (2-20 keV) using the *Ginga* satellite. The observed spectra are similar to those of low-mass X-ray binaries (LMXBs) but significantly softer than those of X-ray pulsars. The spectra can also be described by a thermal bremsstrahlung model with a temperature of $\sim 8 \cdot 10^7$ K,

suggesting that a major fraction of the X-ray emission may originate from very hot gas. As the time scale for starburst activity is significantly shorter than the typical lifetime of LMXBs, Ohashi et al. find it unlikely that the high X-ray luminosity of M83 is caused by LMXBs and instead favour the idea that hot gas (both within and outside of SNRs) produces their observed X-ray spectra.

In this paper we report X-ray observations of M83 carried out with the *ROSAT* X-ray telescope (Trümper 1983, Aschenbach 1988) Position Sensitive Proportional Counter (PSPC, Pfeffermann et al. 1987). The foreground Galactic X-ray-absorbing gas is distributed smoothly across the optical extent of M83 (Hartmann & Burton 1996) and has a relatively low column density ($3.97 \cdot 10^{20}$ cm^{−2}; Dickey & Lockman 1990). Hence our observations allow the detection of diffuse soft (0.1-0.4 keV) X-ray emission due to hot gas in M83. In Section 2 we give the observational details and data analysis. In Section 3 we discuss the different emission components and investigate the interaction of hot gas, galactic winds and magnetic fields. Finally, we compare M83 with other nearby galaxies where diffuse X-ray emission was detected.

2. Observations and data analysis

The data analysis and reduction was performed using the EXtended Scientific Analysis System EXSAS (Zimmermann et al. 1994).

The field of view of the *ROSAT* PSPC detector was centered at the pointing position RA = 13^h37^m00^s.0, Dec

$= -29^{\circ}52'12''.0$ (J2000) so that the X-ray emission of M83 was contained well within the innermost $6'$ from the center. A total of 16 PSPC pointings in the period from Jan 1992 to Jan 1993 (see Table 2) resulted in a 25 ksec integration time.

Table 2. *ROSAT* PSPC observations of M83

Observing interval (OBI)	Date of observation	Time (s)
01	1992 Jan 28	644
02	1992 Aug 09	1363
04-08	1993 Jan 08-09	8291
09,11-18	1993 Jan 10-11	15073

To investigate the data quality and positional offsets, we produced maps of the X-ray emission for each observing interval separately. Comparing the X-ray backgrounds in the individual maps, we looked for contamination due to solar and auroral X-ray photons or due to particles of the cosmic background emission (Snowden & Freyberg 1993, Snowden et al. 1994). Selection of data with low background values (< 20 cts per 60 sec interval) reduced the finally analysed time to 21 ksec but decreased the background noise by $\sim 20\%$.

We looked for positional offsets between X-ray sources in the individual maps and found them to be less than $\sim \pm 10''$. Systematical shifts between the maps could not be found.

The absolute position of the field depends on the accuracy of the PSPC pointing and has been checked comparing point-like X-ray emission features with the positions of stars or extragalactic sources. Checking the positions of stars in the Hubble Space Telescope Guide Star Catalog no identification was obtained. Using the extragalactic database NED² yielded two identifications: the X-ray source at RA $\sim 13^{\text{h}}38^{\text{m}}43^{\text{s}}$, Dec $\sim -29^{\circ}33'5''$ (J2000) is at the position of the F5V star HR 5128 (SAO 181825) which was already detected in the *Einstein* survey (Schmitt et al. 1985). A second identification may exist for X-ray Source 14 (see Table 4) and the quasar MS1332.6-2935. However, the positional uncertainties of these *ROSAT*-detected sources are large because of their large off-axis positions ($29'.0$ and $26'.6$, respectively). We could identify several *ROSAT* X-ray sources in the field of our observations with faint blue stellar objects on “ESO Quick Blue” plates. Details of source identifications will be given in Section 2.2. No systematic positional offsets could be found,

² The NASA/IPAC extragalactic database (NED) is operated by the Jet Propulsion Laboratory, Caltech, under contract with the National Aeronautics and Space Administration

and we decided not to apply any “boresight” corrections for the analysis reported in this paper.

2.1. Derivation of X-ray images

Binning the data to a pixel size of $5''$ we produced images of the inner $40'$ region of the PSPC detector window. These have been exposure-corrected and smoothed in 8 energy subbands (0.11-0.19, 0.20-0.41, 0.42-0.51, 0.52-0.69, 0.70-0.90, 0.91-1.31, 1.32-2.01 and 2.02-2.35 keV). The smoothing was done with a Gaussian filter with full width at half maximum (FWHM) corresponding to the average resolution of the point spread function (PSF) at the detector center in the individual energy subbands. Then the subbands were merged again to form five standard energy bands (cp. Vogler et al. 1996). Table 3 gives the selected *ROSAT* energy bands, FWHMs of the Gaussians used for smoothing, sigma (standard deviation) and background values of the maps computed in ‘source-free’ regions. (We note that - as our observations are photon limited - sigma does not give the real background noise in the maps).

Figure 1 shows a contour plot of the broad-band emission of the whole inner $40'$ field-of-view of the PSPC. Around the extended emission of M83, several previously unknown X-ray point-sources and diffuse emission from a cluster of galaxies in the north-east are visible.

In Fig. 2 we show the contours of the broad-band X-ray emission of the inner part of the PSPC superimposed onto a digitized deep optical image from the 3.9-m Anglo Australian Telescope, reproduced by courtesy of the Anglo Australian Observatory. A number of point-like sources distributed throughout the plane of M83 and complex extended emission centered on, and filling almost the whole optically visible area of the galaxy, are evident.

Figure 3 gives the contour plots for the S (a), H1 (b) and H2 (c) *ROSAT* energy bands (see Table 3) to study the energy dependence of the X-ray emission in more detail.

2.2. Source detection and identification

Source detection and position determination have been performed in the inner $40'$ region of the *ROSAT* PSPC detector field of view where the FWHM of the point response function of the X-ray telescope/PSPC system is smaller than $100''$. For better spectral sensitivity the source detections have been carried out separately in the five *ROSAT* energy bands. Details of these EXSAS detection procedures are given in Pietsch et al. (1994).

We detected a total of 47 sources with a likelihood of existence ≥ 10 (see Table 4 and Figs. 1 and 2). The likelihood is defined as $(-\ln(1 - P))$ where P is the probability that the observed distribution of photons originates from a spurious background fluctuation which in turn is calculated from Poisson statistics. The source counts and

Table 3. Characteristics of the M83 maps

ROSAT energy band			FWHM of Gaussians for smoothing (")	sigma (10^{-6} cts s $^{-1}$ arcmin $^{-2}$)	Background
Broad	B	(0.1-2.4 keV)	52, 38, 28, 25	308	1440
Soft	S	(0.1-0.4 keV)	52, 38	190	1002
Hard	H	(0.5-2.0 keV)	28, 25	221	386
Hard1	H1	(0.5-0.9 keV)	28, 25	149	258
Hard2	H2	(0.9-2.0 keV)	25	151	138

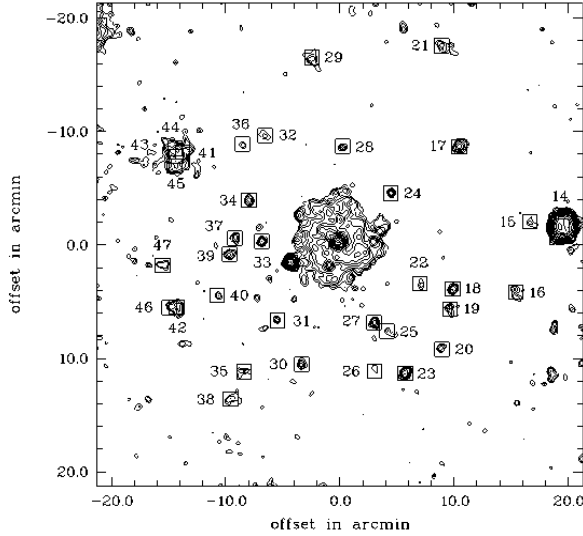


Fig. 1. Contour plot of the broad-band *ROSAT* PSPC image of the inner 40' of the M83 field. The image has been combined from images in the individual energy bands which have been smoothed with a Gaussian filter, with the FWHM of the average PSPC point response function and exposure-corrected for the respective energy bands. Contour levels increase by $2^{n/2}$. Contours are $(1, 1.4, 2, 2.8, 4, \dots) \times 1 \cdot 10^{-3}$ cts s $^{-1}$ arcmin $^{-2}$ above the background (FWHM and background values are given in Table 3). *ROSAT*-detected sources outside of M83 are plotted as squares, with *ROSAT* source numbers. Offsets are with respect to the center of the observation RA = 13^h37^m00^s.0, Dec = -29°52'12".0 (J2000). North is at top, and west to the right

its 1- σ errors are determined by the maximum likelihood method (cp. Zimmermann et al. 1994). They are background subtracted (using the smoothed background image created by cutting out sources with a cut-out radius of 1.5 FWHM at that position and performing a bicubic spline fit to the so-called cheesed image) but not corrected for mirror efficiency (vignetting).

Only those 13 sources inside of M83 which were not flagged as extended by the detection algorithms were accepted and displayed in Fig. 2. The detection of point sources inside the diffuse X-ray emission of M83 is difficult and the likelihood values of these sources might be underestimated. It is worth mentioning that the soft point source at RA \sim 13^h37^m15^s, Dec \sim -29°55'4" (J2000) is

detected with a likelihood value of 7 only, although it is clearly visible in Fig. 3 (a).

Table 4 gives the parameters of all *ROSAT*-detected and accepted X-ray sources. The position errors (Col. 5) of the sources have been calculated in the energy band with the highest likelihood at the 90% confidence radius. The likelihood obtained for the sources are given in Col. 6 together with the corresponding energy band in Col. 7. The counts from the sources in that band are listed in Col. 8. Count rates in the broad band, now corrected for exposure and vignetting, are given in Col. 9.

The count-to-energy conversion factor for e.g. a 5 keV thermal bremsstrahlung spectrum, corrected for Galactic foreground absorption in the direction towards M83, is $1.75 \cdot 10^{-11}$ erg cm $^{-2}$ cts $^{-1}$. Under this assumption a 1 ·

Table 4. X-ray parameters of sources detected in 40'x40' field centered on M83

#	ROSAT name	RA(J2000)	Dec(J2000)	Error	Lik. of exist.	in band	Net counts in that band	Count rates in broad band (10^{-3}s^{-1})
(1)	(2)	(^h ^m ^s) (3)	([°] ['] ^{''}) (4)	(^{''}) (5)	(6)	(7)	(8)	(9)
1	RX J133644-2950.9	13:36:44.1	-29:50:59	9	14	H2	18.2 ± 5.3	1.5±0.4
2	RX J133646-2951.9	13:36:46.5	-29:51:55	6	33	H	54.0 ± 9.4	3.0±0.6
3	RX J133649-2952.7	13:36:49.7	-29:52:46	10	10	H2	25.7 ± 7.5	2.1±0.6
4	RX J133656-2948.1	13:36:56.6	-29:48:06	13	16	H1	19.0 ± 5.2	0.5±0.4
5	RX J133659-2949.9	13:36:59.6	-29:49:54	7	25	H	52.0 ± 9.9	3.0±0.6
6	RX J133700-2951.8	13:37:00.7	-29:51:50	2	478	H	753.3 ± 34.8	40.1±1.9
7	RX J133701-2953.4	13:37:01.4	-29:53:24	8	13	H	38.3 ± 9.5	2.5±0.6
8	RX J133704-2951.3	13:37:04.3	-29:51:20	9	20	H	74.0 ± 14.2	4.0±0.8
9	RX J133704-2953.9	13:37:04.6	-29:53:59	5	45	H	82.0 ± 11.9	4.5±0.7
10	RX J133705-2952.9	13:37:05.8	-29:52:56	10	11	H	31.9 ± 8.5	2.0±0.6
11	RX J133707-2950.8	13:37:07.3	-29:50:51	7	23	H	58.3 ± 11.1	3.2±0.7
12	RX J133716-2949.5	13:37:16.6	-29:49:31	11	114	S	186.4 ± 14.7	2.6±0.5
13	RX J133719-2953.6	13:37:19.9	-29:53:38	3	1143	H	355.7 ± 19.2	21.9±1.1
14	RX J133530-2950.5	13:35:30.5	-29:50:31	2	4201	B	1962.7 ± 46.0	107.6±2.5
15	RX J133543-2950.1	13:35:43.2	-29:50:06	18	10	H	17.2 ± 5.4	1.3±0.5
16	RX J133548-2956.3	13:35:48.9	-29:56:20	20	20	H2	18.2 ± 5.3	2.1±0.5
17	RX J133611-2943.5	13:36:11.8	-29:43:32	10	66	H	54.1 ± 8.3	4.5±0.6
18	RX J133614-2956.0	13:36:14.3	-29:56:02	7	68	H	42.5 ± 7.0	3.1±0.5
19	RX J133615-2957.8	13:36:15.5	-29:57:50	14	27	H	29.5 ± 6.4	2.4±0.5
20	RX J133618-3001.3	13:36:18.8	-30:01:22	14	31	H	26.1 ± 6.0	1.9±0.5
21	RX J133619-2934.6	13:36:19.0	-29:34:37	26	12	H	17.3 ± 5.3	2.3±0.5
22	RX J133627-2955.5	13:36:27.7	-29:55:34	15	15	H	20.3 ± 5.7	1.4±0.4
23	RX J133633-3003.4	13:36:33.6	-30:03:29	7	116	H	68.3 ± 8.9	4.2±0.6
24	RX J133639-2947.6	13:36:39.4	-29:47:39	8	33	H	27.5 ± 5.8	2.0±0.4
25	RX J133641-2959.8	13:36:41.0	-29:59:48	14	11	H	13.7 ± 4.5	1.1±0.4
26	RX J133645-3003.3	13:36:45.9	-30:03:18	20	27	H2	17.0 ± 4.8	1.3±0.5
27	RX J133646-2959.0	13:36:46.1	-29:59:02	7	51	H	39.6 ± 7.0	2.9±0.5
28	RX J133658-2943.5	13:36:58.9	-29:43:30	10	24	H2	16.3 ± 4.4	1.8±0.4
29	RX J133711-2935.6	13:37:11.3	-29:35:40	15	31	H	45.7 ± 8.4	2.3±0.6
30	RX J133715-3002.7	13:37:15.4	-30:02:43	11	41	H	31.9 ± 6.5	2.0±0.5
31	RX J133725-2958.8	13:37:25.2	-29:58:50	12	15	H2	11.8 ± 3.8	1.2±0.4
32	RX J133730-2942.5	13:37:30.2	-29:42:31	19	11	H	18.1 ± 5.5	1.7±0.5
33	RX J133731-2951.8	13:37:31.5	-29:51:52	7	44	H	34.4 ± 6.6	2.4±0.4
34	RX J133736-2948.2	13:37:36.7	-29:48:15	9	39	H	36.5 ± 6.9	2.3±0.5
35	RX J133738-3003.3	13:37:38.9	-30:03:21	14	23	H	26.6 ± 6.3	1.6±0.5
36	RX J133739-2943.3	13:37:39.4	-29:43:18	16	13	H	18.2 ± 5.3	1.2±0.4
37	RX J133742-2951.5	13:37:42.4	-29:51:34	8	44	H	36.0 ± 6.7	2.3±0.5
38	RX J133744-3005.7	13:37:44.2	-30:05:47	25	11	H	18.3 ± 5.6	1.5±0.5
39	RX J133744-2952.9	13:37:44.6	-29:52:59	10	39	H	33.5 ± 6.5	2.5±0.5
40	RX J133749-2956.6	13:37:49.6	-29:56:38	19	13	H	19.8 ± 5.6	1.3±0.4
41	RX J133803-2943.9	13:38:03.4	-29:43:59	12	38	H2	140.0 ± 14.7	7.8±0.9
42	RX J133806-2957.6	13:38:06.0	-29:57:38	13	43	H	49.9 ± 8.4	4.0±0.7
43	RX J133806-2944.3	13:38:06.1	-29:44:22	10	161	H	298.2 ± 20.4	17.8±1.3
44	RX J133806-2943.6	13:38:06.6	-29:43:40	9	78	H	128.7 ± 13.4	7.1±0.8
45	RX J133806-2945.2	13:38:06.8	-29:45:12	10	67	H	103.6 ± 12.1	6.1±0.8
46	RX J133809-2957.6	13:38:09.2	-29:57:41	19	10	B	50.8 ± 13.0	2.7±0.7
47	RX J133811-2953.9	13:38:11.6	-29:53:59	17	21	H	30.3 ± 6.9	1.9±0.5

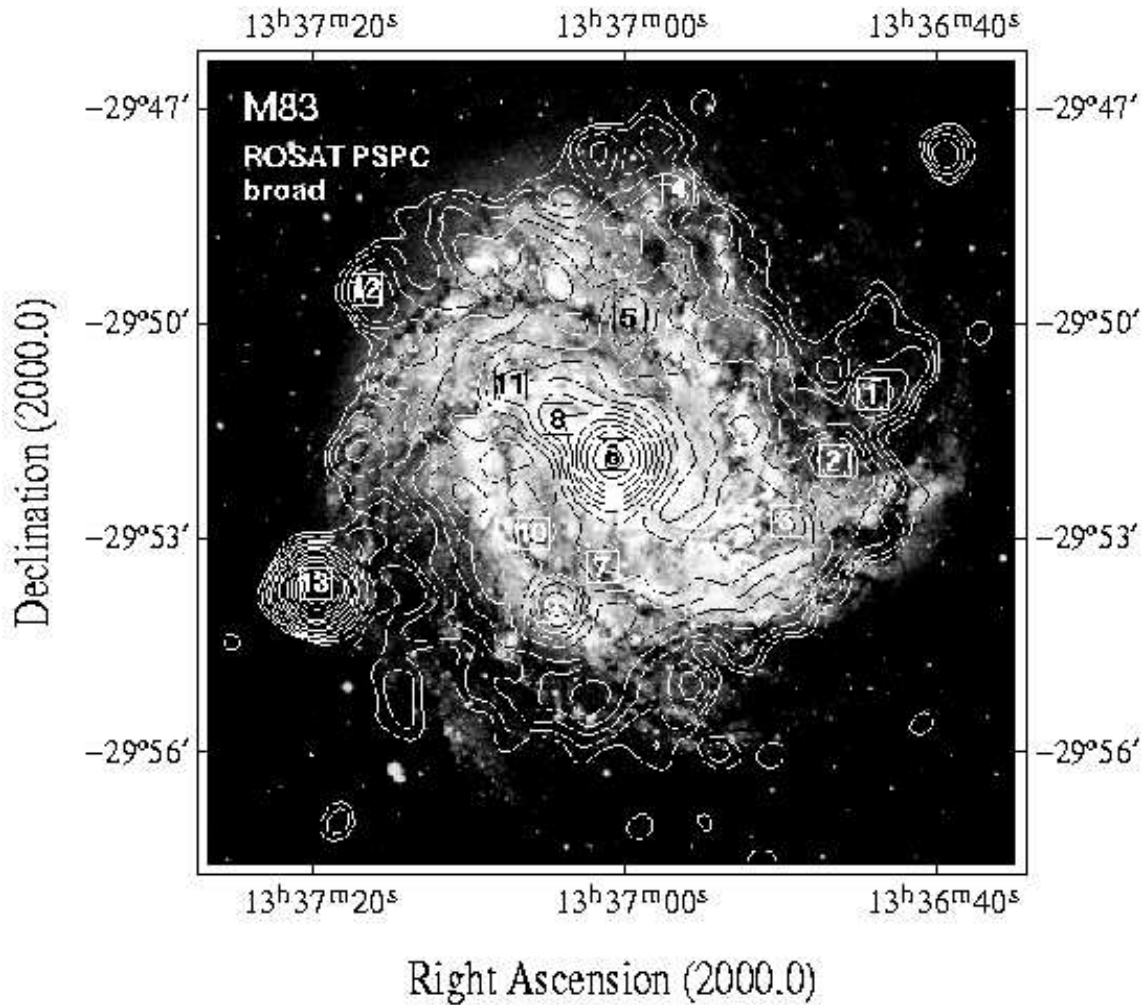


Fig. 2. Broad-band *ROSAT* PSPC contours as in Fig. 1 overlaid onto a deep optical image from the 3.9m Anglo Australian Telescope, kindly provided by David Malin. Here we are showing only the central part of the PSPC field of view. *ROSAT*-detected sources in M83 are marked as squares

10^{-3} cts s^{-1} source at the distance of M83 would have an X-ray luminosity in the broad *ROSAT* energy band of $1.66 \cdot 10^{38}$ erg s^{-1} .

Outside the 40' detection area two more strong X-ray sources are visible at RA $\sim 13^h38^m43^s$, Dec $\sim -29^\circ33'5''$ (partly visible in the upper left corner of Fig. 1) and RA $\sim 13^h34^m58^s$, Dec $\sim -29^\circ55'3''$ (J2000). Due to the large off-axis angles these positions have large errors ($\sim 2'$). The first of these sources can be identified as the F5V star HR 5128 (see above) which was already detected as the *Einstein* Source I8. The second one corresponds to *Einstein* Source I9 (Trinchieri et al. 1985) where it was interpreted as probably a 9th magnitude star.

The starburst nucleus of M83 was detected as an extended X-ray Source 6 and is the strongest source in that galaxy. Its X-ray position coincides very well with the central radio continuum source at RA = $13^h37^m00^s25$, Dec = $-29^\circ51'51''3$ (J2000) (Condon et al. 1982).

We searched for X-ray emission from cataloged historical supernovae in M83 (Richter & Rosa 1984, and references therein): no enhanced X-ray emission at the positions of the radio detections of SN1923a, SN1950b, SN1957d, SN1968l and SN1983n was found in any of the *ROSAT* energy band images.

We also compared the *ROSAT*-detected sources with earlier *Einstein* observations, maps of H α , H I emission (Tilanus & Allen 1993) and optical ESO-SRC plates (Table 5).

2.3. Spatial analysis of the extended emission

Besides the detected X-ray sources, M83 shows complex extended X-ray emission in all *ROSAT* energy bands (see Fig. 3) covering essentially the whole optically visible galaxy.

The S-band contours are rather smooth and (neglecting Source 13 and the source at RA $\sim 13^h37^m15^s$, Dec

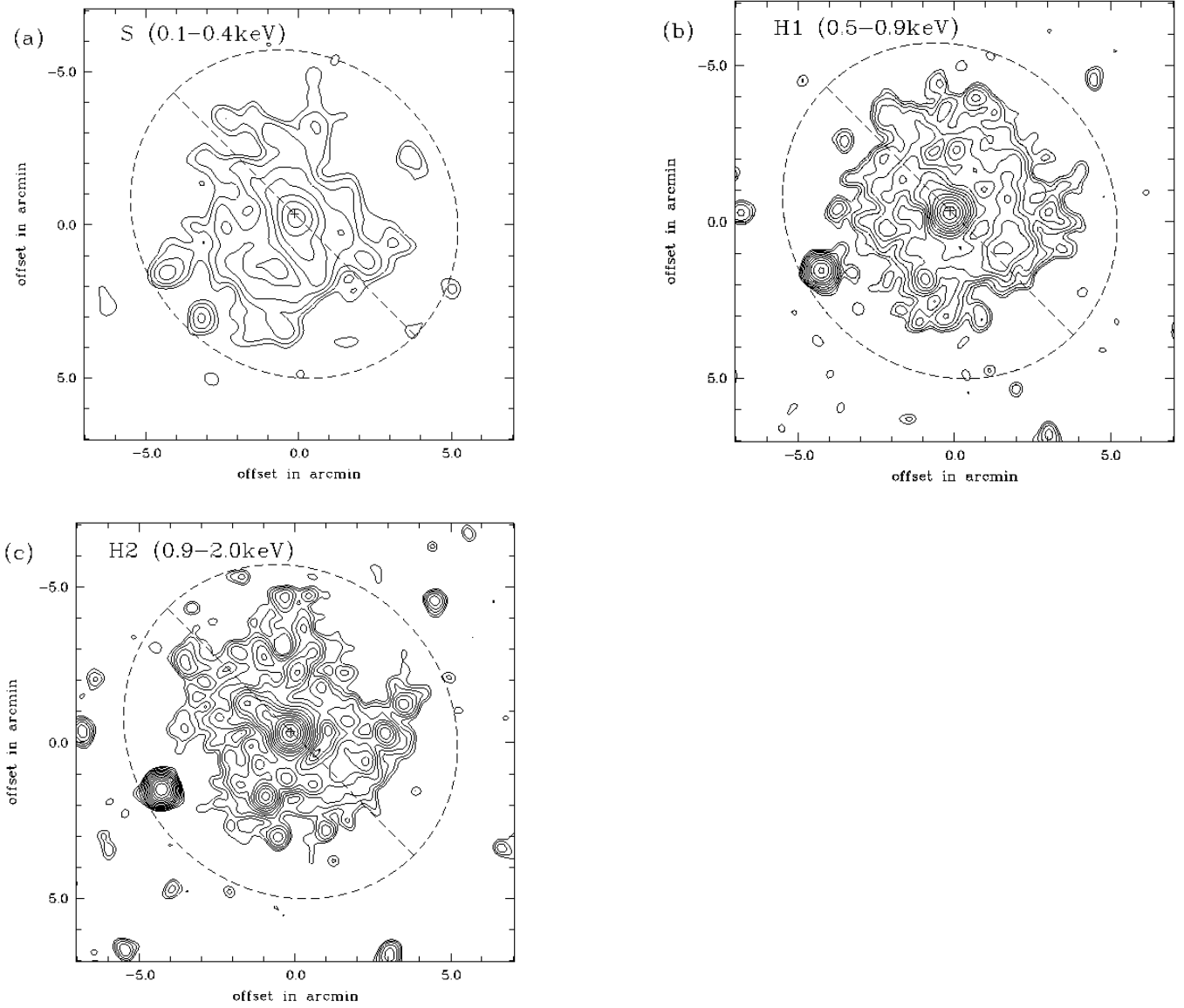


Fig. 3. Contour plots of the emission region of M83 for the S (a), H1 (b) and H2 (c) *ROSAT* PSPC bands. The images have been smoothed and exposure-corrected for the individual bands. Contours are $(1, 1.4, 2, 2.8, 4, \dots) \times 5 \cdot 10^{-4} \text{ cts s}^{-1} \text{ arcmin}^{-2}$ above the background. FWHM and background values are given in Table 3. The dashed ellipse shows the optical extent of the galaxy (D_{25}), and the dashed line the position of the major axis. The position of the central *ROSAT* Source 6 is marked by a cross

$\sim -29^{\circ}55'4$, see Fig. 2) probably do not contain a significant contribution from point sources because their soft X-ray emission is absorbed within the galactic disk of M83. In the H1- and H2-band the point sources are more clearly visible. This is partly caused by the harder spectra of the point sources but also because of the higher spatial resolution of the PSPC at these energies.

2.3.1. Comparison with *Einstein* HRI observations

The soft emission shows a central ridge structure starting from the nucleus in directions P.A. $\sim 40^{\circ}$ as well as

P.A. $\sim 195^{\circ}$ (Fig. 3a). In contrast, the hard emission from this inner part of the galaxy is strongly asymmetric with respect to the central nuclear source: the north-eastern part of the ridge structure is still visible, but the south-western protrusion disappears. Here in the H1 band we see a reduction in the emission that becomes even more visible in the H2 band. In addition, the northern spur observed in the H2 band is pointing to a slightly different direction (P.A. $\sim 55^{\circ}$, Fig. 3b, c).

To study the central region at higher angular resolution, we reanalysed *Einstein* HRI observations (using data

Table 5. Point Source Identification in and around M83

Sources in M83		
Source	Luminosity ^a	Environment and Comments
1	2.5 ± 0.6	H I hole, at the edge of an H II region
3	3.5 ± 1.0	at the edge of an H II region
4	0.8 ± 0.7	at the edge of an H II region
5	5.0 ± 1.0	near H I hole
6	66.6 ± 3.2	nucleus, H I in absorption, H II region, T: <i>Einstein</i> Source H1 ($\Delta RA=2''$, $\Delta Dec=6''$), $L_x(0.5-3.0 \text{ keV}) = 113 \cdot 10^{38} \text{ erg s}^{-1}$, C: radio position ($6''$, $1''$)
7	4.2 ± 1.0	H I hole
8	6.6 ± 1.3	T: <i>Einstein</i> Source H4 ($0''$, $-2''$), $L_x(0.5-3.0 \text{ keV}) = 13 \cdot 10^{38} \text{ erg s}^{-1}$
9	7.5 ± 1.2	H II region, CRB: near therm. radio Source 8 ($19''$, $3''$)
11	5.3 ± 1.2	H II region
13	36.4 ± 1.8	H I in absorption, T: <i>Einstein</i> Sources I2 ($10''$, $-2''$) $L_x(0.5-3.0 \text{ keV}) = 39 \cdot 10^{38} \text{ erg s}^{-1}$ or H2 ($3''$, $8''$) $L_x(0.5-3.0 \text{ keV}) = 24 \cdot 10^{38} \text{ erg s}^{-1}$, ESO-SRC plates: diffuse faint object
Sources around M83		
Source	Flux ^a	Environment and Comments
14	188.3 ± 4.4	T: <i>Einstein</i> Source I6 ($8''$, $4''$) $f_x(0.5-3.0 \text{ keV}) = 3.2 \cdot 10^{-12} \text{ erg cm}^{-2} \text{ s}^{-1}$, G: AGN MS1332.6-2935
16	3.7 ± 0.9	ESO-SRC plates: several objects
23	7.4 ± 1.1	ESO-SRC plates: diffuse faint object
27	5.1 ± 0.9	ESO-SRC plates: diffuse faint object
28	3.2 ± 0.7	ESO-SRC plates: faint object
41,43-45	67.9 ± 3.3	T: <i>Einstein</i> Source I7 (background cluster, $z=0.189$, $H_0 = 50 \text{ km/s Mpc}$) $L_x(0.5-3.0 \text{ keV}) = 7.0 \cdot 10^{43} \text{ erg s}^{-1}$, $L_x(0.1-2.4 \text{ keV}) = (19.4 \pm 0.5) \cdot 10^{43} \text{ erg s}^{-1}$ ESO-SRC R-plate: $\gtrsim 3$ diffuse objects (nothing visible on J-plate)
42,46	11.7 ± 1.8	ESO-SRC plates: two faint objects

^a - Assuming $kT=5 \text{ keV}$, $N_H = 3.97 \cdot 10^{20} \text{ cm}^{-2}$, distance to M83=8.9 Mpc. Luminosities in units of $10^{38} \text{ erg s}^{-1}$, fluxes in $10^{-14} \text{ erg cm}^{-2} \text{ s}^{-1}$

^b - T: Trinchieri et al. 1985; C: Condon et al. 1982; CRB: Cowan et al. 1994; G: Gioia et al. 1990

obtained through the High Energy Astrophysics Science Archive Research Center Online Service, provided by the NASA Goddard Space Flight Center) which were already published by Trinchieri et al. (1985). We combined the two *Einstein* observations (1980 Jan 15-16: 24575 s & 1981 Feb 13: 20003 s) after correcting for a positional offset, aligned them with our *ROSAT* maps and used adaptive filtering (cf. Ehle et al. 1995) to produce a new map which is displayed in Fig. 4 as a contour plot.

In the *Einstein* image we identify the north-eastern spur and the two emission peaks that are visible in the H2 band emission (Fig. 3c). It is worth mentioning that we do not detect *Einstein* Source H3 in any of our *ROSAT* energy bands and therefore conclude that this source is variable. The *Einstein* HRI contour plot shows emission extending from the nucleus in a south-western direction (P.A. $\sim 208^\circ$), similar to the ridge structure in the soft image, but its radial extent is much smaller, probably owing to lack of sensitivity. Slightly enhanced X-ray emission south of the nuclear region is visible in the H1 band and

is probably associated with the south-western spur that is visible in the *Einstein* observations as well.

2.3.2. Radial and azimuthal distribution of the diffuse X-ray emission

To quantify the distribution of the diffuse X-ray emission in our *ROSAT* maps, we subtracted the detected point-like sources and integrated the remaining diffuse emission separately in the north-western and south-eastern half of M83 out to a galactic radius of $5'$. The two halves were separated by the galaxy's major axis. While the emission in the two hard bands is enhanced in the north-western part by about 3% relative to the south-eastern part, the soft-band emission shows the opposite asymmetry, with a lack of soft emission in the north-western half of M83 (decreased by about 3%).

In order to investigate if the diffuse X-ray emission of M83 originates from sources that are also responsible for the production of cosmic rays (as was suggested by Fabiano et al. (1982) in the case of peculiar galaxies) we compared the extent of the radio continuum (Neininger

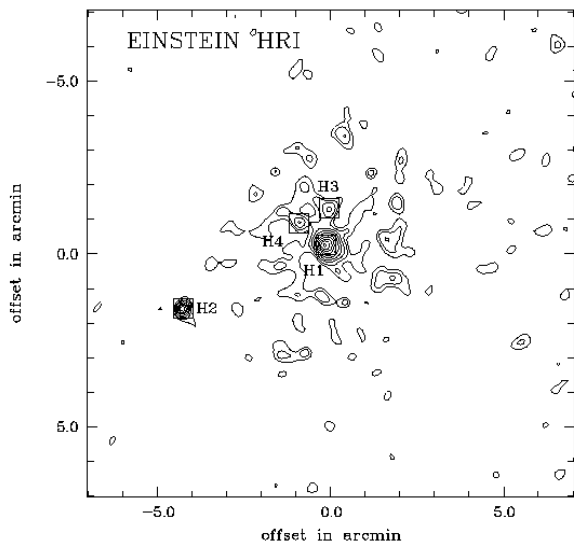


Fig. 4. *Einstein* HRI contours of M83, adaptively filtered with Gaussian functions of $\text{FWHM} \leq 8''.6$ and aligned with our *ROSAT* observations. Contours of $(1, 1.4, 2, 2.8, 4, \dots) \times 3\sigma$ above the background are plotted (cp Fig. 4 in Trinchieri et al. (1985)). Positions of the *Einstein* -HRI-detected sources are marked as squares

1992) and the diffuse X-ray emission. Figure 5 gives the radial profiles of the extended X-ray emission for the soft and hard energy range, calculated by averaging counts in rings of $12''$ (0.5 kpc) which are centered on the position of the central X-ray source. Whereas the soft emission is smoothly decreasing with radius, the profile of the hard emission component has a local minimum at ~ 4 kpc (corresponding to the reduction in the emission south-west of the nucleus (cp. Fig. 3c)) followed by an enhancement. This local maximum is also visible as a distinct ‘hump’ in the radial distribution of the optical surface brightness (Talbot et al. 1979) where this region was found to contain the bluest light in the galaxy outside the nucleus. The radio continuum profiles at $\lambda 2.8$ cm (Neininger 1992), however, are very smooth over the whole radial extent of M83.

The scale length of the extended hard-band X-ray emission outside a radius of 5.5 kpc is $l_x = 3.4 \pm 0.3$ kpc (neglecting the nuclear region with $l_x = 1.1 \pm 0.2$ kpc as

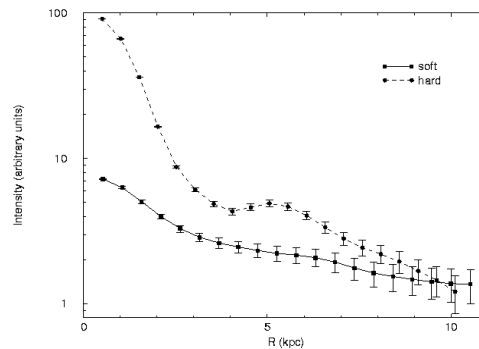


Fig. 5. Radial profiles of the extended component of the X-ray emission of M83. The plot gives the intensities (in arbitrary units) in circular annuli around the central source for the soft and hard energy range, separately

well as circular annuli around the local minimum at ~ 4 kpc). The scale length of the $\lambda 2.8$ cm radio emission is $l_{\text{syn}} \sim 4.4$ kpc. Neininger (1992) separated the thermal and nonthermal radio continuum emission of M83 and calculated for the thermal emission at $\lambda 2.8$ cm a scale length of $l_{\text{th}} \sim 3.2$ kpc, consistent with that of the hard-band diffuse X-ray emission.

An important finding is that the radial profile of the soft diffuse X-ray emission shows a much larger scale length that is best fitted with a Gaussian of half FWHM $\sim 10 - 15$ kpc. In addition, the ‘hump’ in the profile of the hard X-ray emission does not exist in the soft energy image.

2.3.3. Separation of emission components

We calculated the count rates and hardness ratios (defined as hardness ratio 1 $\text{HR1} = (\text{hard} - \text{soft}) / (\text{hard} + \text{soft})$ and hardness ratio 2 $\text{HR2} = (\text{hard2} - \text{hard1}) / (\text{hard2} + \text{hard1})$, see Table 6) for the diffuse emission of M83. The extended emission in the different energy bands was integrated over a ring with an inner radius of $1'$ and outer radius of $5'$ and corrected for the background and time of exposure. The same was done for the nuclear region with radius $1'$ separately. The definition of the extent of the nuclear region is somewhat arbitrary, and it results from the qualitative inspection of the contour maps. We should note that this and all following calculations making use of the so called ‘diffuse emission’ are based on upper limits of this emission component. Part of it may be due to sources below our detection threshold (cf. Sect. 3.1).

To determine the emission resulting from detected point-like sources, we added up the count rates in the different energy bands as they were obtained from our source detection (Table 6). The total X-ray emission of

Table 6. Components of the X-ray emission from M83

Emission component	Count rates 10^{-3} cts s $^{-1}$	Hardness ratios	
		HR1	HR2
Nuclear region	103 ± 2	0.76 ± 0.02	0.03 ± 0.02
Extended emission	197 ± 4	0.49 ± 0.03	-0.10 ± 0.02
Point-like sources	29 ± 2	0.34 ± 0.05	0.28 ± 0.07
Total emission	329 ± 5	0.56 ± 0.02	-0.02 ± 0.02

M83 is dominated by the complex extended emission in all *ROSAT* energy bands. All detected sources (excluding the nuclear Source 6 and Source 13) contribute only 9% to the total count rate. The hardness ratios show that the point-like sources in general have hard spectra and that the nuclear emission is harder than the extended emission.

2.4. Spectral analysis: derivation of X-ray colors and fits to models

Nearly all sources (1, 2, 4-11) in M83 are most likely bright X-ray binaries showing strong absorption of the soft-band flux as expected from their position in the galactic disk of M83. Source 12 shows enhanced soft X-ray emission. The very strong X-ray source 13 might be an AGN, a quasar, or a radio galaxy. Only this source and the nucleus are strong enough to allow a detailed spectral analysis. The best fit to Source 13 is a thermal plasma spectrum with N_{H} fixed to the Galactic foreground value, yielding a temperature of $(3.1 \pm_{0.6}^{2.4}) \cdot 10^7$ K and a flux density of $(3.5 \pm 1.4) \cdot 10^{-13}$ erg cm $^{-2}$ s $^{-1}$ (errors correspond to the 68.3% confidence level of our best fit with $\chi^2/\nu = 0.68$ and 14 degrees of freedom).

A more detailed spectral analysis of other single point sources is very difficult because of the unknown contribution of the underlying diffuse emission.

To study the spectra of the diffuse extended X-ray emission we excluded circular regions (with a radius $1.5 \times$ FWHM of the point response function) at the positions found by our source detection. Source 13 was excluded because it is most likely a background source. We also excluded the central part of M83 (radius $1' \hat{=} 2.6$ kpc around the position of the central Source 6) which we shall discuss as the nuclear region in Sect. 2.4.1. The remaining emission, integrated out to a galactic radius of $5' \hat{=} 12.9$ kpc is discussed as extended emission in Sect. 2.4.2. Background values were derived by integrating counts in nearby emission-free regions. The resulting count rate spectra were binned so that each energy interval had a signal-to-noise ratio larger than 5.

2.4.1. Nuclear region

The background subtracted energy spectrum of the photons originating from the nuclear area cannot be fitted

with sufficient statistical reliability by simple spectral models, like a power-law, a thermal bremsstrahlung or a thin thermal Raymond-Smith model with ‘cosmic’ abundances (Raymond & Smith 1977). Details of the used models are given by Zimmermann et al. (1994). Table 7 lists the fit results. Furthermore, for the thermal plasma model the best-fit foreground absorption is too low compared to the Galactic foreground value. However, an acceptable fit is produced by the combination of a thermal Raymond-Smith plasma of temperature T_1 with an internally absorbed thermal plasma of temperature T_2 , both affected by Galactic foreground absorption. Again, the model assumed ‘cosmic’ abundances to reduce the number of free parameters (see Table 7 for best-fit parameters and Fig. 6). As the largest uncertainties of the fit come both from the dependence of T_1 and T_2 as well as from that between T_1 and the internal absorption ($N_{\text{H}}^{\text{int}}$), Fig. 7 shows confidence contours for these two sets of parameters.

The physical motivation for a two-component thermal plasma model is the expectation that one observes a superposition of a soft halo and hard disk emission in face-on galaxies, as is supported by studies of edge-on galaxies like NGC 4631 (Wang et al. 1995, Vogler & Pietsch 1996) and NGC 253 (Pietsch 1993) where the differentiation of disk and halo regions is possible. Our best-fit model explains the X-ray emission originating from a warm gas component ($0.18 \pm_{0.01}^{0.02}$ keV $\hat{=} 2.1 \cdot 10^6$ K; probably located in the halo region) and hot plasma ($0.45 \pm_{0.13}^{0.24}$ keV $\hat{=} 5.2 \cdot 10^6$ K; probably the hot gas near to the nucleus and in the disk of M83). The harder X-ray emission from the hot gas component is strongly internally absorbed. This agrees with the result that the nuclear region shows a significantly higher HR1 than the point-like sources and the extended emission. Using the best-fit parameters, the X-ray luminosity of the M83 nuclear region in the broad *ROSAT* band is $L_{\text{x}} = 1.6 \cdot 10^{40}$ erg s $^{-1}$ (53% due to the cooler and 47% due to the hotter gas component). The luminosity of the diffuse soft component is $L_{\text{x}}(\text{soft}) = 0.4 \cdot 10^{40}$ erg s $^{-1}$ and originates almost only from the lower-temperature plasma. The soft X-ray luminosity is used to estimate the physical parameters of the emitting gas in Sect. 3.3.

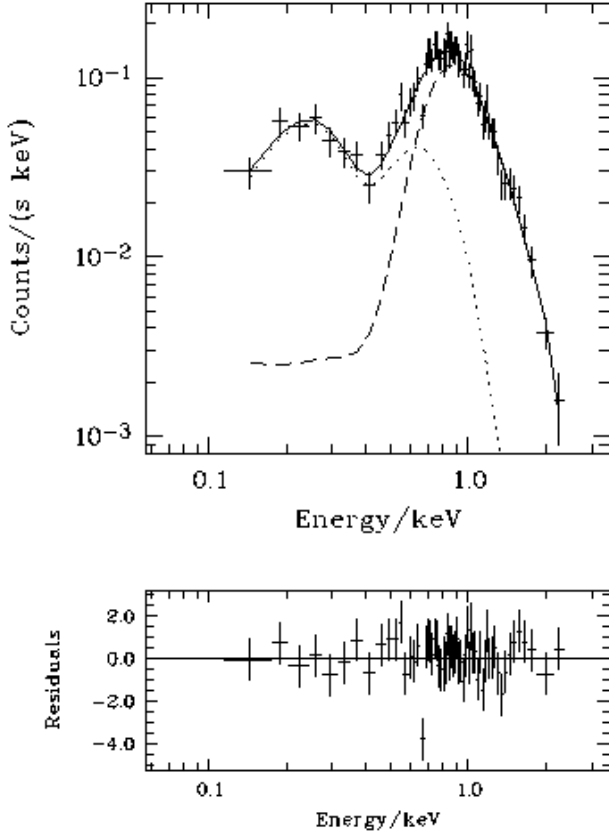


Fig. 6. Observed *ROSAT* PSPC spectrum of the nuclear area of M83 between 0.1 and 2.4 keV (the 2200 photons are divided in 63 bins) together with the two-temperature fit (see Table 7). The contribution of the low-temperature component is indicated separately as the dotted and that of the high-temperature component as the dashed curve. The lower part of the diagram shows residuals in units of standard deviations

2.4.2. Diffuse soft emission due to hot gas

We assume that, after subtraction of the detected sources and the nuclear area, the remaining broad-band emission of M83 is a mixture of hot thermal gas (in the disk and in the halo) and weak hot sources that might not be detected in the present observations. Trying to fit the observed photon spectra with simple models again gave no acceptable results. However, the combined two-temperature spectral model already discussed for the nuclear region yields a good description of the observed spectra. The best-fit parameters for the extended emission are given in Table 7.

Again the best-fit is obtained by combining a soft X-ray emitting warm ($0.18 \pm_{0.01}^{0.02}$ keV $\hat{=}$ $2.1 \cdot 10^6$ K) plasma with an internally absorbed hot ($0.49 \pm_{0.16}^{0.23}$ keV $\hat{=}$ $5.7 \cdot 10^6$ K) gas (see Table 7 and Fig. 8). Figure 9 shows the confidence contours for this spectral fit. The X-ray luminosity of the M83 extended diffuse emission in the *broad*

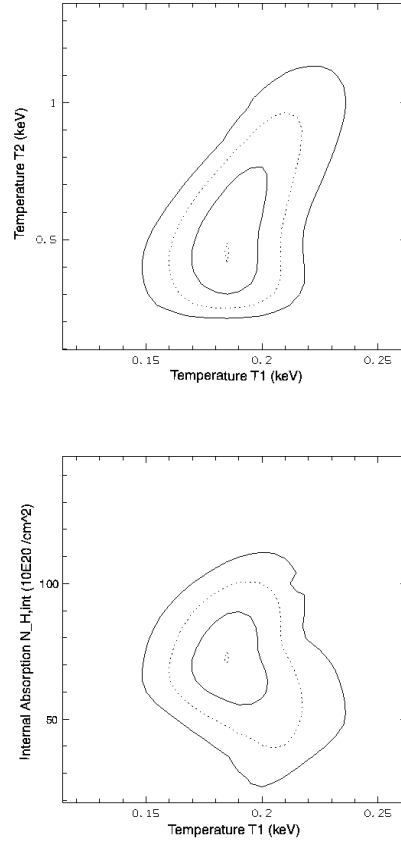


Fig. 7. χ^2 contours for the model fit (a combination of a thermal Raymond-Smith plasma of temperature T_1 with an internally absorbed thermal plasma of temperature T_2 , both affected by Galactic foreground absorption) to the spectrum of the nuclear area of M83. The region of the χ^2 minimum is indicated by the inner dashed contour followed by contours corresponding to 68.3%, 96.5% and 99.7% confidence levels. The number of “interesting parameters” (cf. Avni 1976) is three. The *top* panel shows the plot of the parameter set T_1 and T_2 , the *bottom* that of T_1 and $N_{\text{H}}^{\text{int}}$

ROSAT band then is $L_{\text{x}} = 3.6 \cdot 10^{40}$ erg s $^{-1}$ (75% due to the warm and 25% due to the hot gas component). The X-ray luminosity in the soft energy band, computed for the best-fit parameters, is $L_{\text{x}}(\text{soft}) = 1.4 \cdot 10^{40}$ erg s $^{-1}$ and originates almost completely from the cooler gas component, as it is the case for the nuclear area (see above).

3. Discussion

3.1. Point-like sources

We detected 13 point-like sources in M83, 10 of which were previously unknown, down to a limiting sensitivity of $\sim 0.8 \cdot 10^{38}$ erg s $^{-1}$. Four of the seven *Einstein* detected sources could not be found again and are probably time-variable X-ray binaries. The number of background

Table 7. Spectral parameters of the nuclear area and extended emission of M83. Errors are corresponding to the 68.3% confidence levels

Model	$N_{\text{H}}^{(a)}$		Index	$kT^{(b)}$		$\nu^{(c)}$	χ^2/ν	$L_{\text{x}}(\text{soft})^{(d)}$
	external	internal		kT_1	kT_2			
Nuclear Area								
Thermal bremsstrahlung	$6.8\pm_{0.4}^{0.5}$		$3.0\pm_{0.1}^{0.1}$	$0.60\pm_{0.04}^{0.04}$		60	2.1	
Power-law	$9.6\pm_{0.4}^{0.5}$					60	2.7	
Raymond-Smith	$1.1\pm_{0.2}^{0.2}$			$0.94\pm_{0.03}^{0.07}$		60	1.7	
Raymond-Smith ^(e)	3.97			$0.93\pm_{0.02}^{0.09}$		61	4.3	
Two-temp. Raymond-Smith ^(e)	3.97	$72.7\pm_{7.8}^{6.6}$		$0.18\pm_{0.01}^{0.02}$	$0.45\pm_{0.13}^{0.24}$	58	0.9	0.4
Extended Emission								
Thermal bremsstrahlung	$5.3\pm_{0.4}^{0.3}$		$3.6\pm_{0.1}^{0.2}$	$0.44\pm_{0.02}^{0.03}$		58	1.2	
Power-law	$8.7\pm_{0.7}^{0.6}$					58	1.6	
Raymond-Smith	$1.0\pm_{0.4}^{0.4}$			$0.37\pm_{0.02}^{0.05}$		58	4.1	
Raymond-Smith ^(e)	3.97			$0.30\pm_{0.01}^{0.03}$		59	5.5	
Two-temp. Raymond-Smith ^(e)	3.97	$75.4\pm_{9.4}^{10.6}$		$0.18\pm_{0.01}^{0.02}$	$0.49\pm_{0.16}^{0.23}$	56	0.9	1.4

(a) in units of 10^{20} cm^{-2}

(b) in units of keV

(c) numbers of degrees of freedom

(d) luminosity in the soft (0.1-0.4 keV) energy range (for a M83 distance of 8.9 Mpc), corrected for Milky Way absorption, in units of $10^{40} \text{ erg s}^{-1}$ (e) external N_{H} fixed to Galactic value

sources in the X-ray emitting area of M83 at our limiting luminosity is expected to be only 1.2, based on the luminosity function of sources from the *ROSAT* medium-sensitivity survey (Hasinger et al. 1991). We note that this value represents an upper limit as the absorbing material in the disk of M83 further reduces the chance to detect background sources.

Eight of the detected X-ray sources in M83 are positionally correlated with H II regions and/or H I voids and could be giant bubbles of hot gas in star-forming regions, young supernova remnants (Marston et al. 1995), ultraluminous X-ray binaries or a combination of all these components (Williams & Chu 1995). Such a coincidence of X-ray sources and H I holes has been detected in the face-on galaxy M51 (Ehle et al. 1995) and M101 (Snowden & Pietsch 1995, Williams & Chu 1995). Kamphuis et al. (1991) showed for one of the holes in M101 that it is indeed associated with an expanding H I shell. Diffuse X-ray emission from hot gas in H I shells also was found within the LMC (Chu & Mac Low 1990; Wang & Helfand 1991; Bomans et al. 1994). The resolved shells in the LMC, however, only reach X-ray luminosities of about $10^{37} \text{ erg s}^{-1}$, factors of more than 10 less than the one required for the M83 point sources. This indicates that hot gas confined in a giant bubble can not explain the high X-ray luminosity of these sources. A more detailed discussion of time variability, properties of individual sources and a comparison with H I channel maps should make use of sensitive

ROSAT HRI observations of M83 (Blair, in prep.) which allow a more reliable source detection and separation of point sources from the surrounding diffuse emission.

Our PSPC observations of M83 allow a crude estimate of the amount of undetected point-like sources contributing to the luminosity of the extended emission (calculated in Sect. 2.4.2). As the number of detected sources in M83 is rather low, the integral luminosity distribution of sources in M31 (a single power-law with slope -0.8; Trinchieri & Fabbiano 1991) is assumed. Furthermore, assuming that only sources above $1 \cdot 10^{34} \text{ erg s}^{-1}$ contribute significantly to the luminosity due to point-like sources (this cutoff is based on observations of X-ray binaries in the Milky Way), we integrated the logN-logS distribution normalized to the total luminosity of detected point-like sources in M83. The luminosity due to undetected plus detected point-like sources is found to be $1.2 \cdot 10^{40} \text{ erg s}^{-1}$, a factor of ~ 2.5 higher than what has been detected. Undetected point-like sources might explain $\sim 20\%$ of the extended diffuse X-ray emission. Supper et al. (1997) found a flattening of the luminosity distribution with decreasing luminosities for the globular cluster sources in M31. If this is true also for point-like sources in M83, the X-ray luminosity due to undetected sources would be even smaller. This result is in good agreement with that from *Ginga* observations, namely that a thermal component is making a considerable contribution in the X-ray emission rather than LMXBs or X-ray pulsars (Ohashi et al. 1990).

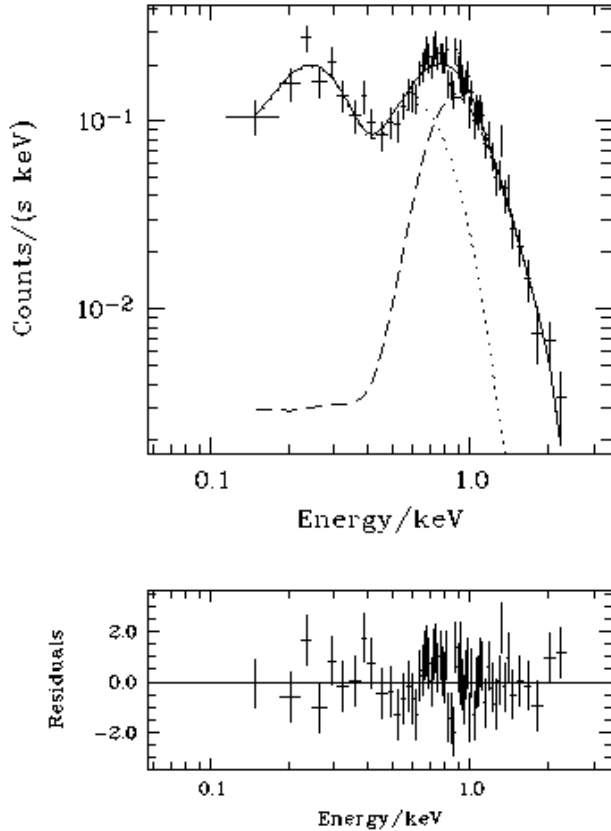


Fig. 8. Observed *ROSAT* PSPC spectrum of the extended emission of M83 between 0.1 and 2.4 keV (the 5600 photons are divided in 61 bins) together with the two-temperature fit (cp. Fig. 6)

3.2. Nuclear region

Earlier *Einstein* IPC observations could not be used to investigate the spectral properties of the extended and nuclear emission of M83 because of the short exposure time (~ 6000 s) and detector gain variations (Trinchieri et al. 1985). Spectral observations of M83 with the *Ginga* satellite (Ohashi et al. 1990) also do not allow a separation of the nuclear emission from the remaining diffuse emission because of their low angular resolution. Spectral modelling based on *ROSAT* observations, however, tells us that the nuclear X-ray emission is complex. The nucleus itself is detected as a bright point-like source by our source detection algorithm and shows a relatively hard spectrum. The *ROSAT* observed luminosity of the nuclear region of M83 is $L_x(0.1-2.4 \text{ keV}) \sim 1.6 \cdot 10^{40} \text{ erg s}^{-1}$, in agreement with the *Einstein* observations within the range of uncertainties ($L_x(0.5-3.0 \text{ keV}) \sim 1.1 \cdot 10^{40} \text{ erg s}^{-1}$) and can be compared with other known starburst nuclei, such as NGC 7714 ($L_x(\text{Einstein}) = 6 \cdot 10^{40} \text{ erg s}^{-1}$; Weedman et al. 1981), NGC 253 ($L_x(\text{Einstein}) = 1.7 \cdot 10^{39} \text{ erg s}^{-1}$; Fabiano & Trinchieri 1984, scaled to 2.58 Mpc distance), and

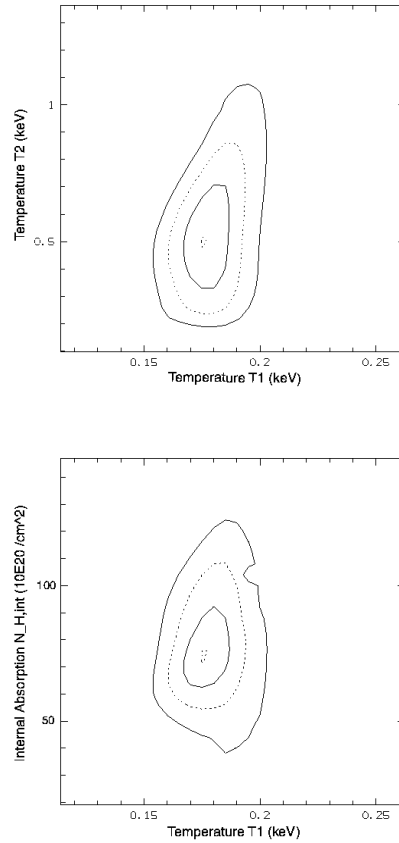


Fig. 9. χ^2 contours for the model fit (a combination of a thermal Raymond-Smith plasma of temperature T_1 with an internally absorbed thermal plasma of temperature T_2 , both affected by Galactic foreground absorption) to the spectrum of the extended emission of M83. The region of the χ^2 minimum is indicated by the inner dashed contour followed by contours corresponding to 68.3%, 96.5% and 99.7% confidence levels. The number of “interesting parameters” (cf. Avni 1976) is three. The *left* panel shows the plot of the parameter set T_1 and T_2 , the *right* that of T_1 and $N_{\text{H}}^{\text{int}}$

NGC 1808 ($L_x(\text{ROSAT}) = 1.4 \cdot 10^{41} \text{ erg s}^{-1}$; Junkes et al. 1995).

A comparison of the observed spectra of the nuclear area and the disk (Figs. 6 and 8) shows that in the nuclear region the emission of the hard component is stronger than that of the soft component, in contrast to the extended disk and halo emission of M83 where both spectral components contribute equally. The harder spectral properties of the emission from the nuclear area are also visible in the different hardness ratios (see Table 6).

The soft X-ray emission of the nucleus of M83 (Fig. 3a) is clearly extended and shows a ridge-like structure pointing approximately in the direction of the optically visible bar. Neininger et al. (1991) showed that the magnetic field

also follows closely that bar structure, favouring the idea of a link between the hot gas and magnetic fields.

However, the reason for the strong asymmetry of the hard nuclear X-ray radiation (Fig. 3b and c) is still unclear: No such asymmetrical emission features are detected at any other wavelengths. We do not expect that the nuclear hard X-ray protrusion results from very hot gas emerging from the nucleus and travelling through the relatively dense galactic disk. Instead we prefer the idea that the asymmetry is due to point-like sources distributed asymmetrically around the galactic nucleus. These sources are not resolved by the spatial resolution of the PSPC-detector and might be connected to strong star-forming regions. We will have to wait for sensitive M83 *ROSAT* HRI observations (Blair, in prep.) to study the structure and origin of the extended nuclear X-ray emission in more detail. Part of the extended nuclear emission of M83 might well be resolved into point-like bulge sources, as it is the case for the nucleus of M51 (Immler 1996).

3.3. Extended emission

If we account for diffusion of cosmic rays away from their sites of origin, the synchrotron scale length should be larger than that of the extended X-ray emission which is in agreement with our observations. The same result was found for the galaxy M51 (Ehle et al. 1995). The agreement of the scale length of the hard-band diffuse X-ray- and of the thermal radio emission favours the idea that the hard diffuse emission is due to hot gas produced by star-forming regions in the galactic disk. This hypothesis is further supported by the fact that the ‘hump’ at ~ 5 kpc is also visible in the optical light where it indicates the presence of active and recent star formation (Talbot et al. 1979).

The smooth profile of the soft, diffuse X-ray emission together with its shallow radial descent argue for the idea that this X-ray emission component is related to a different distribution of emitting sources. From observations of the H I velocity field (Tilanus & Allen 1993) and under the assumption of trailing spiral arms, it follows that the north-western part of the galactic disk is nearer to the observer. Hence, the asymmetric distribution of the soft X-rays supports the existence of a spherical gas halo: the galactic disk is opaque to soft X-rays so that we only see the emission from the front hemisphere. The asymmetric distribution of surface brightness (Sect. 2.3.2) is explainable as a projection effect caused by the galactic inclination and absorption (cp. Pietsch et al. 1994).

The idea that most of the soft X-ray emission is due to hot gas located in a huge halo above the disk of M83 is further supported by the spectral characteristics of the diffuse emission: The X-ray spectrum of the extended emission is complex and cannot be described by simple models. This is understandable, as observing a face-on galaxy like M83 must result in a superposition of different X-ray emission

components from the disk and halo that are affected by internal absorption from the H I gas distribution in the galactic disk. This statement is supported by X-ray observations of edge-on galaxies where these components can be viewed separately in and above the disk. We note, however, that only observations of face-on galaxies allow the study of the distribution of X-ray emission with respect to the (underlying) disk. Our best fit (with a reasonably small amount of free parameters) is a two-temperature Raymond-Smith plasma with both internal and external absorption, the latter fixed to the H I column density of the Milky Way in the direction to M83. A similar two-temperature model was found to give a good description of the diffuse X-ray emission from NGC 4631 (Wang et al. 1995). As these authors, we expect not only two discrete temperatures but probably a continuous temperature distribution in the real disk and halo gas. In future, more sophisticated spectral models in combination with X-ray telescopes, offering higher energy resolution, might allow a better description.

If the diffuse X-ray emission in the soft energy band is assumed to be due to hot halo gas, it is possible to calculate the gas density n_e , mass m_{gas} and cooling time τ of that plasma. To this end we use the model of thermal cooling and ionization equilibrium of Nulsen et al. (1984) where $L_x(\text{soft}) = 1.11 \cdot \Lambda(T) n_e^2 V \eta$. The unknown filling factor η allows for some clumpiness of the gas. For the gas temperatures of the nuclear region and of the extended halo emission ($\sim 2.1 \cdot 10^6$ K) Raymond et al. (1976) give a cooling coefficient $\Lambda(T)$ of $\sim 10 \cdot 10^{-23}$ erg cm³ s⁻¹. To calculate the physical parameters of the hot gas component one has to make assumptions about the emitting volume V : here we take into account that the soft diffuse X-ray emission from regions behind the disk of M83 is absorbed by the neutral hydrogen in the galactic disk. Column densities of $\sim 0.5 \cdot 10^{21}$ cm⁻² already lead to a nearly complete absorption of the soft-band emission. Such and even higher N_H values are observed in the disk of M83 (Tilanus & Allen 1993). We assume that the nuclear soft X-ray radiation is emitted from a hemisphere with radius $1'$ (see above) and that the extended soft emission from the halo of M83 fills a hemisphere with radius $5' \triangleq 13$ kpc (see above), minus a cylinder of radius $1'$ around the center where the emission clearly is dominated by the gas of the nuclear area. The calculated gas parameters are presented in Table 8.

The total mass of the detected hot gas (nuclear area plus halo) is $2.2 \cdot 10^8 \sqrt{\eta} M_\odot$ which is only $\lesssim 0.2\%$ of the total gas mass (cp. Table 1). Similarly low mass contributions are found for the galaxies M51 (Ehle et al. 1995) and NGC 1566 (Ehle et al. 1996). The cooling times are longer than the time scale for starburst activity which is estimated to be around $\sim 10^7$ yr (Rieke et al. 1988, Trinchieri et al. 1985).

Table 8. Halo Gas Parameters for M83

Region	n_e (cm^{-3})	m_{gas} (M_{\odot})	τ (yr)
Nuclear area	$7.0 \cdot 10^{-3} / \sqrt{\eta}$	$0.1 \cdot 10^8 \cdot \sqrt{\eta}$	$0.5 \cdot 10^8 \cdot \sqrt{\eta}$
Rest of M83	$1.2 \cdot 10^{-3} / \sqrt{\eta}$	$2.1 \cdot 10^8 \cdot \sqrt{\eta}$	$2.8 \cdot 10^8 \cdot \sqrt{\eta}$

3.4. Hot gas, galactic winds and magnetic fields

From X-ray observations of the hot gas it is possible to calculate the thermal energy density of this component of the interstellar medium: $U_{\text{therm}} = n_e k_B T$. (It is, however, still not clear whether the ions are in thermal equilibrium with the plasma electrons (see Lesch 1990) and how strongly they contribute to U_{therm}). A comparison of the nuclear area and the halo region of M83 (Table 8) shows that U_{therm} is a factor of 6 higher in the nuclear region. Here the gas can escape much more easily from the galactic disk and rise up into the halo, e.g. in the form of a galactic wind channeled by vertical magnetic fields (Breitschwerdt & Schmutzler 1994). High Faraday rotation measures and strong depolarization of polarized radio emission in the central part of M83 support this concept (Neininger et al. 1991, Ehle 1995). Further evidence of nuclear gas outflow comes from the detection of absorption lines blueshifted by 1000 km s^{-1} relatively to the system's velocity (Bohlin et al. 1983).

Whereas the electron densities of the hot gas (as derived from the presented X-ray data) are in general too low to explain the observed depolarization (see below), the density in the nuclear area is relatively high and may contribute to the Faraday effects. A comparison of the polarized radio emission at $\lambda 20 \text{ cm}$ and the broad-band diffuse X-ray emission (Fig. 10) shows indeed a correlation of strong X-ray emission with low polarized intensities in the central area of M83. This may indicate that the diffuse X-ray emitting hot gas in the nuclear area depolarizes by the effect of internal Faraday dispersion along the line of sight, produced by turbulent magnetic fields and thermal gas inside the emitting source (Burn 1966, Ehle & Beck 1993). Adopting a strength of the turbulent magnetic field of $25 \mu\text{G}$ (Neininger et al. 1993), a pathlength of $1' \hat{=} 2.6 \text{ kpc}$ (see above) and a typical turbulence scale length of 50 pc requires electron densities of $\sim 2 \cdot 10^{-2} / \sqrt{\eta} \text{ cm}^{-3}$ to explain the depolarization of $DP \sim 0.02$ at $\lambda 20 \text{ cm}$ in the central region of M83. This gas density is comparable, within the range of uncertainties, to that calculated from our X-ray observations (see Table 8).

The electron densities of thermal gas in the galactic halo required to explain the strong depolarization outside the nuclear area are in the range of $n_e \gtrsim 0.03 \text{ cm}^{-3}$

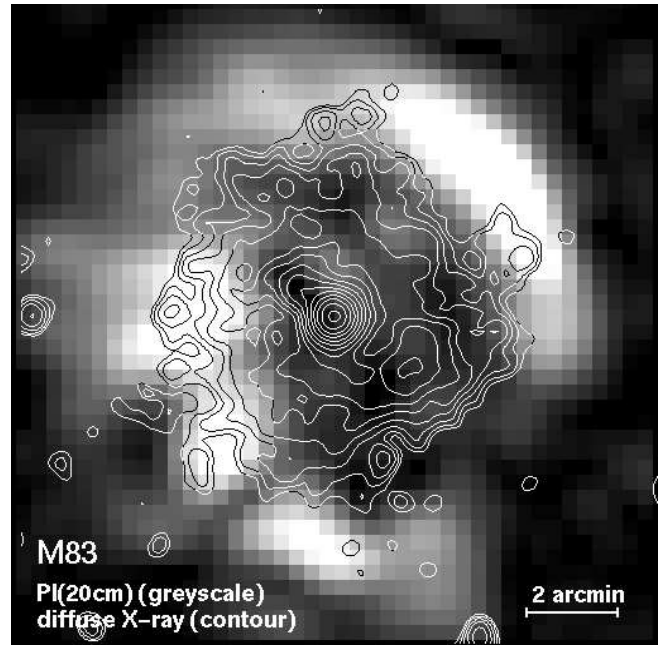


Fig. 10. Broad-band *ROSAT* PSPC contours of the diffuse X-ray emission of M83 (detected point sources are subtracted), overlaid onto a greyscale map of the distribution of polarized intensity at $\lambda 20 \text{ cm}$ (cp. Sukumar & Allen 1989). Contours are $(1, 1.4, 2, 2.8, 4, \dots) \times 1 \cdot 10^{-3} \text{ cts s}^{-1} \text{ arcmin}^{-2}$ above the background

(e.g. Ehle 1995). These values are *inconsistent* with the halo densities as derived from our *ROSAT* X-ray observations. Either Faraday depolarization occurs in cooler ionized gas not radiating in X-rays (warm absorber), or the turbulence scale length in the halo is much larger than in the disk, or the assumption of ionization equilibrium (Raymond-Smith plasma with one specific temperature) is not valid. The latter possibility is supported by the model of galactic winds and delayed recombination (Breitschwerdt & Schmutzler 1994). In their simulation the soft X-ray emission can be explained by a cooler (typical 10^4 K) gas which might have electron densities that are larger by a factor 3-5 (Schmutzler, priv. comm.) than the values given in Table 8.

From radio polarization observations it is possible to compare U_{therm} with the energy density of the magnetic field: $U_{\text{magn}} = B^2 / 8\pi$. Assuming equipartition between cosmic rays and magnetic fields, Neininger et al. (1993) calculated, for a synchrotron emitting disk of $1.0 \pm 0.5 \text{ kpc}$ thickness, a total magnetic field strength of $B = 11 \pm 2 \mu\text{G}$ for M83. To scale the disk field strength to that of the halo we use observations of the edge-on galaxy NGC 253 (Beck et al. 1994) where the field strength at a height of $z \sim 2.5 \text{ kpc}$ above the galactic disk is found to be about 80% of the disk value.

Allowing the filling factor to vary between 0.1 and 0.8 and including a 0.1 keV uncertainty for the gas tempera-

ture, we obtain a rough estimate of the plasma parameters $\beta = U_{\text{therm}}/U_{\text{magn}}$ of 0.2 ± 0.1 both for the nuclear area and for the halo. The galactic wind model (see above) leads to an even lower β .

Although there are other contributions to the total energy density of the hot interstellar medium (e.g. turbulent motions, cosmic rays) it is obvious that the magnetic field plays an important role for galactic haloes. How it might channel galactic winds, support or hinder the escape of hot gas from the galactic disk, or heat the gas via MHD waves or magnetic reconnection is still under discussion.

3.5. Comparison with other galaxies

Assuming that most of the mechanical energy supplied to the interstellar gas is from supernovae, one might ask whether this energy input is high enough to explain the thermal energy of the hot X-ray emitting gas (cf. Fabiano et al. 1997). Based on an idealized model for the X-ray emission (a single spherical expanding bubble, cf. Heckman et al. 1996), the supernova rate of M83 ($0.29 - 0.49 \text{ yr}^{-1}$; see below) might produce a thermal energy of $(1.3 - 2.2) \cdot 10^{56} \text{ erg}$ integrated over a typical starburst period of 10^7 yr . This value is indeed above the thermal energy of the hot gas in the halo region of $\sim 0.4 \cdot 10^{56} \sqrt{\eta} \text{ erg}$, using the same assumptions for the volume of the emitting halo and the soft-band X-ray luminosity as in Sect. 3.3. This agreement between model and observations supports the hypothesis that the diffuse X-ray emission arises from hot gas originally heated by supernovae.

The luminosity of the diffuse X-ray emission in M83 of $3.6 \cdot 10^{40} \text{ erg s}^{-1}$ in the broad *ROSAT* energy band is very high. Even if one assumes that only the soft X-ray emission of $1.8 \cdot 10^{40} \text{ erg s}^{-1}$ of the extended and nuclear component originates from a halo above the galactic disk (Sect. 3.3) this component is still much brighter than the halo emission of the edge-on galaxies NGC 4631 ($0.1 - 0.2 \cdot 10^{40} \text{ erg s}^{-1}$; Vogler & Pietsch 1996) or NGC 253, a galaxy well known for its huge X-ray halo ($\sim 0.17 \cdot 10^{40} \text{ erg s}^{-1}$; Pietsch et al. 1997).

Not only is the absolute value of the X-ray luminosity of the diffuse component in M83 high but it also strongly dominates the total emission. Even if we take into account that 20% of the so-called diffuse emission from the disk area could in fact be point-like sources below the detection-limit of $0.8 \cdot 10^{40} \text{ erg s}^{-1}$ (Sect. 3.1), the fraction of diffuse emission in M83 is 78% of the total luminosity, comparable to the corresponding value of 70% for NGC 253 (see Table 9). Values for NGC 253 are based on results of the data analysis by Pietsch et al. (1997) and Vogler et al. (1997) for an assumed distance of 2.58 Mpc.

Although the luminosities of the emission components in M83 are much higher than that of NGC 253 - a fact partly explainable by the still uncertain extragalactic distances - there is an agreement of the relative contributions to the total luminosity. The (distance-independent) mean

Table 9. Comparison of X-ray luminosities of emission components in M83 and NGC 253

luminosity in $10^{40} \text{ erg s}^{-1}$	M83		NGC 253	
total	5.7	100%	0.46 ^a	100%
halo ^b	1.8	32%	0.17	37%
disk + bulge, diffuse ^c	2.7	47%	0.15	33%
disk + bulge, point-like sources	1.2 ^d	21%	0.14	30%

^a - only half of the total halo emission is included for comparison with the face-on galaxy M83

^b - assuming that the soft diffuse emission originates from the halo

^c - the remaining part of the diffuse emission is assumed to be present in the disk and bulge. For M83 it is reduced by 20% to account for undetected point-like sources

^d - for M83 we give the sum of detected plus estimated undetected point-like sources

surface brightness I_x of the soft diffuse emission of M83 is about twice that of NGC 253 (Table 10). In edge-on view the X-ray halo of M83 would probably look even more spectacular than that of NGC 253.

To search for a common reason for this difference between M83 and NGC 253 we compare these two galaxies with other galaxies where diffuse X-ray emission is detected. We do this with respect to their supernova rates and discuss also distance-independent parameters like the X-ray surface brightnesses I_x and the energy input per surface area, $\dot{E}_{\text{A}}^{\text{tot}}$, a quantity that measures the activity in the galactic disk and seems to be important for the evolution of galactic radio haloes (Dahlem et al. 1995, Dumke et al. 1995, Golla 1997). Results for four galaxies are presented in Table 10.

The supernova rates and consequently the energy input rates into the interstellar medium are well correlated with the X-ray surface brightnesses. The energy input rate in case of M83 is very high and even higher than that for NGC 253 (if averaged over the whole area of star formation). The energy input rate from the inner star-forming disk of NGC 253 alone is by far the highest, a result that might explain the extreme vertical extent of the X-ray halo emission of that galaxy.

While there is increasing evidence that star formation activity in the disks of spiral galaxies is related to the existence and structure of radio haloes, further studies are needed to test the correlation between the energy input by supernovae in the disk and the surface brightness and evolution of X-ray haloes. Future X-ray satellites, with their higher spatial resolution and sensitivity especially for the soft X-ray component, will help to disentangle the emission of hot gas in haloes and disks.

Table 10. Comparison of M83 and other galaxies with diffuse X-ray emission

Galaxy (1)	D (2)	r_{SF} (3)	$\nu_{\text{SN}}^{\text{nt}}$ (4)	$\nu_{\text{SN}}^{\text{FIR}}$ (5)	$\dot{E}_{\text{A}}^{\text{tot}}$ (6)	I_{x} (7)
M83	8.9	9.9	0.29	0.49	3.2	2.9
NGC 253	2.58	7.7 2.3 [†]	0.11	0.15	1.9 22.7	1.5
NGC 3628	6.7	7.0	0.04	0.06	0.9	1.0
NGC 4565	9.7	16.9	0.02	0.04	0.1	0.5

† - in NGC 253 most of the star formation is limited to the inner disk (Scoville et al. 1985: extended inner stellar disk)

(2) - assumed distance in Mpc

(3) - radial extent of star-forming disk in kpc, estimated from IRAS CPC observations (van Driel et al. 1993)

(4) - supernova rate in yr^{-1} , calculated from the power of non-thermal radio emission using formulae given by Dahlem et al. (1995)

(5) - supernova rate in yr^{-1} , calculated from FIR luminosities given by Young et al. (1989)

(6) - mean energy input rate per unit surface area (as defined in Dahlem et al. 1995) in $10^{-3} \text{ erg s}^{-1} \text{ cm}^{-2}$

(7) - X-ray surface brightness in $10^{-6} \text{ erg s}^{-1} \text{ cm}^{-2}$, calculated over the area of soft halo emission in NGC 253, NGC 3628 and NGC 4565 and over the extent of the soft diffuse emission in M83, respectively.

An important finding of our study is that outflow models for the transport of hot gas up into the halo should not be restricted to nuclear starbursts and superwinds (Suchkov et al. 1994), but should include the whole star-forming galactic disk. M83 is a good example of a X-ray halo produced by an active star-forming disk.

Acknowledgements. We would like to thank David Malin, AAO, for providing the optical image on M83 and Stuart Ryder, Uni. of NSW, for the H α map. Jürgen Kerp, RAIUB, is acknowledged for helpful comments on the manuscript as well as Andreas Vogler, MPE, for his help during the data reduction. Our anonymous referee is acknowledged for numerous helpful suggestions. The work of ME was supported by the *Deutsche Agentur für Raumfahrtangelegenheiten (DARA)* project number 50 OR 9206 and 50 OR 9405 and the *Deutsche Forschungsgemeinschaft (DFG)* grant number Eh 154/1-1. The *ROSAT* project is supported by the German *Bundesministerium für Bildung, Wissenschaft, Forschung und Technologie* and the *Max-Planck-Gesellschaft*.

References

Aschenbach B., 1988, Appl. Opt. 27, 1404
 Avni Y., 1976, ApJ 210, 642
 Beck R., Carilli C.L., Holdaway M.A., Klein U., 1994, A&A 292, 409
 Bohlin R.C., Cornett R.H., Hill J.K., Smith A.M., Stecker T.P., 1983, ApJ 274, L53

Bomans D.J., Dennerl K., Kürster M., 1994, A&A 283, L21
 Breitschwerdt D., Schmutzler T., 1994, Nat 371, 774
 Burn B.J., 1966, MNRAS 133, 67
 Chu Y.-H., Mac Low M.-M., 1990, ApJ 365, 510
 Condon J.J., Condon M.A., Gisler G., Puschell J.J., 1982, ApJ 252, 102
 Cowan J.J., Roberts D.A., Branch D., 1994, ApJ 434, 128
 de Vaucouleurs G., de Vaucouleurs A., Corwin H.G., 1976, Second Reference Catalogue of Bright Galaxies, Univ. of Texas Press, Austin
 Dahlem M., Lisenfeld U., Golla G., 1995, ApJ 444, 119
 Dickey J.M., Lockman F.J., 1990, ARA&A 28, 215
 Dumke M., Krause M., Wielebinski R., Klein U., 1995, A&A 302, 691
 Ehle M., 1995, PhD thesis, University of Bonn
 Ehle M., Beck R., 1993, A&A 273, 45
 Ehle M., Pietsch W., Beck R., 1995, A&A 295, 289
 Ehle M., Beck R., Haynes R.F., Vogler A., Pietsch W., Elmoutie M., Ryder S., 1996, A&A 306, 73
 Fabbiano G., 1988, ApJ 330, 672
 Fabbiano G., Trinchieri G., 1984, ApJ 284, 491
 Fabbiano G., Feigelson E., Zamorani G., 1982, ApJ 256, 397
 Fabbiano G., Trinchieri G., Macdonald A., 1984, ApJ 284, 65
 Fabbiano G., Schweizer F., Mackie G., 1997, ApJ 478, 542
 Gioia I.M., Maccacaro T., Schild R.E., Wolter A., Stocke J.T., Morris S.L., Henry J.P., 1990, ApJS 72, 567
 Golla G., 1997. In: Lesch H., Dettmar R.-J., Mebold U., Schlickeiser R. (eds.) The physics of galactic halos, Akademie Verlag, Berlin, p. 85
 Hartmann D., Burton B.W., 1996, The Leiden-Dwingeloo Atlas of Galactic Neutral Hydrogen, Cambridge Univ. Press
 Hasinger G., Schmidt M., Trümper J., 1991, A&A 246, L2
 Heckman T.M., Dahlem M., Eales S.A., Fabbiano G., Weaver K., 1996, ApJ 457, 616
 Huchtmeier W.K., Bohnenstengel H.-D., 1981, A&A 100, 72
 Immler, S., 1996, Diploma Thesis, University of Munich
 Junkes N., Zinnecker H., Hensler G., Dahlem M., Pietsch W., 1995, A&A 294, 8
 Kamphuis J., Sancisi R., van der Hulst J.M., 1991, A&A 244, L29
 Lesch H., 1990, A&A 239, 437
 Marston A.P., Elmegreen D., Elmegreen B., Forman W., Jones C., Flanagan K., 1995, ApJ 438, 663
 Neininger N., 1992, PhD thesis, University of Bonn
 Neininger N., Klein U., Beck R., Wielebinski R., 1991, Nat 352, 781
 Neininger N., Beck R., Sukumar S., Allen R.J., 1993, A&A 274, 687
 Nulsen P.E.J., Stewart G.C., Fabian A.C., 1984, MNRAS 208, 185
 Ohashi T., Makishima K., Tsuru T., Takano S., Koyama K., Stewart G.C., 1990, ApJ 365, 180
 Pfeffermann E., Briel U.G., Hippmann H., et al., 1987, Proc. SPIE 33, 519
 Pietsch W., 1993, In: Hensler G., Theis Ch., Gallagher J. (eds.) Panchromatic View of Galaxies, p. 137
 Pietsch W., Vogler A., Kahabka P., Jain A., Klein U., 1994, A&A 290, 307
 Pietsch W., et al., 1997, A&A (in prep.)
 Raymond J.C., Smith B.W., 1977, ApJS 35, 419
 Raymond J.C., Cox D.P., Smith B.W., 1976, ApJ 204, 290

- Richter O.G., Rosa M., 1984, *A&A* 140, L1
- Rieke G.H., Lebofsky M.J., Walker C.E., 1988, *ApJ* 325, 679
- Sandage A., Tammann G.A., 1975, *ApJ* 194, 559
- Sandage A., Tammann G.A.: 1987, *A Revised Shapley-Ames Catalog of Bright Galaxies*, Carnegie Institution of Washington Publication 635, Washington D.C., 2nd Edition
- Schmitt J.H.M.M., Golub L., Harnden F.R., et al., 1985, *ApJ* 290, 307
- Scoville N.Z., Soifer B.T., Neugebauer G., Matthews K., Young J.S., Yerka J., 1985, *ApJ* 289, 129
- Snowden S.L., Freyberg M.J., 1993, *ApJ* 404, 403
- Snowden S.L., Pietsch W., 1995, *ApJ* 452, 627
- Snowden S.L., McCammon D., Burrows D.N., Mendenhall J.A., 1994, *ApJ* 424, 714
- Sofue Y., Wakamatsu K.-I., 1994, *AJ* 107, 1018
- Suchkov A.A., Balsara D.S., Heckman T.M., Leitherer C., 1994, *ApJ* 430, 511
- Sukumar S., Allen R.J., 1989, *Nat* 340, 537
- Supper R., Hasinger G., Pietsch W., Trümper J., et al., 1997, *A&A* 317, 328
- Talbot R.J., Jensen E.B., Dufour R.J., 1979, *ApJ* 229, 91
- Tilanus R.P.J., Allen R.J., 1993, *A&A* 274, 707
- Trinchieri G., Fabbiano G., Palumbo G.G.C., 1985, *ApJ* 290, 96
- Trümper J., 1983, *Adv. Space Res.* 2, 241
- van Driel W., de Graauw Th., de Jong T., Wesselius P.R., 1993, *A&AS* 101, 207
- Vogler A., Pietsch W., 1996, *A&A* 311, 35
- Vogler A., Pietsch W., Kahabka P., 1996, *A&A* 305, 74
- Vogler A., et al., 1997, *A&A* (in prep.)
- Wang Q.D., Helfand D.J., 1991, *ApJ* 379, 327
- Wang Q.D., Walterbos R.A.M., Steakley M.F., Norman C.A., Braun R., 1995, *ApJ* 439, 176
- Watson M., Stanger V., Griffiths R.E., 1984, *ApJ* 286, 144
- Weedman D.W., Feldman F.R., Balzano W.A., Ramsey L.W., Sramek R.A., Wu C.-C., 1981, *ApJ* 248, 105
- Williams R.M., Chu Y.-H., 1995, *ApJ* 439, 132
- Wilson A.S., Elvis M., Lawrence A., Bland-Hawthorn J., 1992, *ApJ* 391, L75
- Young J.S., Xie S., Kenney J.D.P., Rice W., 1989, *ApJS* 70, 699
- Zimmermann H.U., Becker W., Belloni T., Döbereiner S., Izzo C., Kahabka P., Schwentker O., 1994, *EXSAS User's Guide*, Edition 4, MPE Report 257